The enhanced alcohol-sensing response of ultrathin WO$_3$ nanoplates

The enhanced alcohol-sensing response of ultrathin WO$_3$ nanoplates

Deliang Chen[1,2,3]**, Xianxiang Hou**[1]**, Hejing Wen**[1]**, Yu Wang**[1]**,
Hailong Wang**[1]**, Xinjian Li**[2]**, Rui Zhang**[1,4]**, Hongxia Lu**[1]**,
Hongliang Xu**[1]**, Shaokang Guan**[1]**, Jing Sun**[3] **and Lian Gao**[3]

[1] School of Materials Science and Engineering, Zhengzhou University, 100 Science Road,
Zhengzhou 450001, People's Republic of China
[2] School of Physics and Engineering, Zhengzhou University, 100 Science Road,
Zhengzhou 450001, People's Republic of China
[3] The State Key Laboratory of High Performance Ceramics and Superfine Microstructure,
Shanghai Institute of Ceramics, Chinese Academy of Sciences, 1295 Dingxi Road,
Shanghai 200050, People's Republic of China
[4] Laboratory of Aeronautical Composites, Zhengzhou Institutes of Aeronautical Industry
Management, University Center, Zhengdong New District, Zhengzhou 450046,
People's Republic of China

E-mail: dlchen@zzu.edu.cn and dlchennano@hotmail.com

Abstract

Chemical sensors based on semiconducting metal oxide nanocrystals are of academic and
practical significance in industrial processing and environment-related applications. Novel
alcohol response sensors using two-dimensional WO$_3$ nanoplates as active elements have been
investigated in this paper. Single-crystalline WO$_3$ nanoplates were synthesized through a
topochemical approach on the basis of intercalation chemistry (Chen *et al* 2008 *Small* **4** 1813).
The as-obtained WO$_3$ nanoplate pastes were coated on the surface of an Al$_2$O$_3$ ceramic
microtube with four Pt electrodes to measure their alcohol-sensing properties. The results show
that the WO$_3$ nanoplate sensors are highly sensitive to alcohols (e.g., methanol, ethanol,
isopropanol and butanol) at moderate operating temperatures (260–360 °C). For butanol, the
WO$_3$ nanoplate sensors have a sensitivity of 31 at 2 ppm and 161 at 100 ppm, operating at
300 °C. For other alcohols, WO$_3$ nanoplate sensors also show high sensitivities: 33 for
methanol at 300 ppm, 70 for ethanol at 200 ppm, and 75 for isopropanol at 200 ppm. The
response and recovery times of the WO$_3$ nanoplate sensors are less than 15 s for all the test
alcohols. A good linear relationship between the sensitivity and alcohol concentrations has been
observed in the range of 2–300 ppm, whereas the WO$_3$ nanoparticle sensors have not shown
such a linear relationship. The sensitivities of the WO$_3$ nanoplate sensors decrease and their
response times become short when the operating temperatures increase. The enhanced
alcohol-sensing performance could be attributed to the ultrathin platelike morphology, the high
crystallinity and the loosely assembling structure of the WO$_3$ nanoplates, due to the advantages
of the effective adsorption and rapid diffusion of the alcohol molecules.

(Some figures in this article are in colour only in the electronic version)

1. Introduction

Chemical sensors based on low dimensional nanostructured
materials show high sensitivity and fast speed of response
to various vapors and gases, and have important applications
in environmental monitoring, medical detection, the food
industry, the mining industry, bioengineering and defense
safety [1–6]. Nanoparticles, nanowires, nanotubes and
nanoplates of metals, metal oxides, carbon and related
compounds have been widely investigated for chemical sensor

use [5–10]. Currently, the development of fast and sensitive gas sensors with small cross-sensitivity is a key subject of intensive research [7]. Improving the performance (e.g., achieving high sensitivity, rapid response and low operating temperature) of the established sensor systems and designing novel sensor concepts on the basis of bottom-up approaches and nanotechnologies are the routes towards the above objective [1–12].

Alcohol sensors with unique performance have numerous practical applications in the areas of wine quality monitoring, breath analysis, and the food and biomedical industries [13, 14]. Semiconducting metal oxides, including SnO_2 nanofibers [15], branched SnO_2 nanowires [16], indium-doped SnO_2 nanowires [17], ZnO nanorods [18], porous ZnO nanoplates [19], ZnO nanotubes [20], TiO_2 nanoparticles [21], porous α-Fe_2O_3 nanorods [22], α-Cr_2O_3 nanotubes [23], porous $ZnFe_2O_4$ nanorods [24], $CdIn_2O_4$ nanocrystals [25], V_2O_5 nanobelts [14], V_2O_5 macroscopic fibers [26], SnO_2/NASICON-type composites [27] and α-Fe_2O_3/SnO_2 core–shell nanorods [28], have been reported as efficient active elements for alcohol-detection applications. However, there are also some problems needing to be solved. For instance, the requirement of elaborate control in synthesizing low dimensional nanocrystals greatly raises the costs, and the raised costs limit the applications of alcohol sensors [23, 28]. In addition, low sensitivities and slow response degrade the performance of alcohol sensors [14, 29]. The lack of selectivity of chemical sensors also impairs the importance in detection. Further endeavors, therefore, need to be made to develop novel alcohol-sensing nanomaterials using cost-effective processes.

Tungsten trioxide (WO_3) and related compounds are useful semiconducting materials with many unique properties [30]. WO_3 nanocrystals with controlled morphologies have been synthesized by various processes, including nanoporous-walled WO_3 nanotubes as highly active visible-light-driven photocatalysis [31], hierarchical WO_3 hollow shells for photocatalytic application [32], aligned WO_3 nanotrees for superhydrophilic thin films [33], and nanoparticles [34]. Recent research results suggest that tungsten oxide nanocrystals, such as Cr-doped WO_3 nanoparticles [35], Cr-doped mesoporous WO_3 [36], single-crystalline WO_3 nanowires [37–39], mat-like networked tungsten oxide nanowire thin films [40], Au and Pd activated WO_3 nanocrystals [41], mixed WO_3–$CuWO_4$ films [42], $WO_{2.72}$ nanorods [43], $WO_{2.72}$ nanowires [44], and WO_3 hollow spheres [45], are potential gas-sensing materials, not only for oxidizing gases (NO_x [46], NO_2 [36, 37, 40, 47, 48], O_3 [41] and O_2 [49]), but also for reducing gases (e.g., NH_3 [43], H_2S [50], CS_2 [45], CO [51], CH_4 [38], hydrocarbon [39], H_2 [44], acetone [35], ethanol [41, 42], and butanol [42]). However, the sensitivity of the reported WO_3-based sensors is not high enough for practical applications and the responses are also sluggish [52]. To improve the sensitivities and shorten the response times of WO_3 sensors, some second nanoparticles are usually necessary as activators [35, 36, 41].

In this paper, we report a novel alcohol sensor with high sensitivities and rapid response using ultrathin single-crystalline WO_3 nanoplates as the active materials for the first time. The WO_3 nanoplates, with superhigh specific surface areas, large diameter-to-thickness ratios and perfect single-crystalline structures, are synthesized via a topochemical transformation process on the basis of intercalation chemistry [53, 54]. The WO_3 nanoplate sensors obtained show superhigh sensitivity to alcohols (e.g., methanol, ethanol, isopropanol and butanol), and their response and recovery times are shorter than 15 s. A linear relationship between the sensitivities and gas concentrations is observed for all of the test alcohols. The possible mechanisms are discussed in some detail.

2. Experimental details

### 2.1. Synthesis of WO_3 nanoplates

Microscale $H_2W_2O_7 \cdot xH_2O$ powders with a size range of 5–15 μm were synthesized according to a process reported before [61]. Tungstate-based inorganic–organic hybrid nanobelts were synthesized using the intercalating reactions between $H_2W_2O_7 \cdot xH_2O$ and *n*-octylamine in a nonpolar medium of heptane [53]. The tungstate-based inorganic–organic hybrid nanobelts were of a layered mesostructure, alternately consisting of inorganic [WO_6] layers and organic ammonium layers [53]. Removal of the organic ammonium layers from the tungstate-based inorganic–organic hybrid nanobelts led to the formation of ultrathin platelike H_2WO_4 nanoplates [54]. The as-obtained H_2WO_4 nanoplates were then calcined at 250, 300, 400 and 500 °C for 2 h in air to synthesize WO_3 nanoplates, and the calcined products at various temperatures are denoted as WO_3-250, WO_3-300, WO_3-400 and WO_3-500, respectively. For the purposes of comparison, commercial H_2WO_4 powders (AR, Sinopharm Chemical Reagent Co., Ltd) were calcined at 550 °C for 2 h to prepare WO_3 nanoparticles.

2.2. Characterization of the WO_3 nanocrystals

XRD patterns were obtained using an X'Pert Pro x-ray diffractometer equipped with Cu Kα radiation. TEM and HRTEM images were recorded on a Tecnai-G 20 transmission electron microscope with an acceleration voltage of 200 kV. SEM images were obtained using a Quanta-200 scanning electron microscope.

2.3. Fabrication of WO_3 sensors

WO_3 nanoplates (or nanoparticles) were mixed with a small amount of de-ionized H_2O to form WO_3 pastes in a glass dish. The WO_3 pastes were then brush-coated onto the surface of an Al_2O_3 microtube with four Pt electrodes (figure 1(a)). After the WO_3 coating was air-dried, the coating process was repeated until a complete coating was formed. The WO_3-coated Al_2O_3 microtube was then fixed to a special pedestal with six poles (figure 1(c)) by welding the four Pt electrodes to four poles of the pedestal. A heating coil (figure 1(b)) was then inserted through the Al_2O_3 microtube and its two ends were welded to the other two poles of the pedestal. A photograph of the as-obtained WO_3 sensor is shown in figure 1(d).
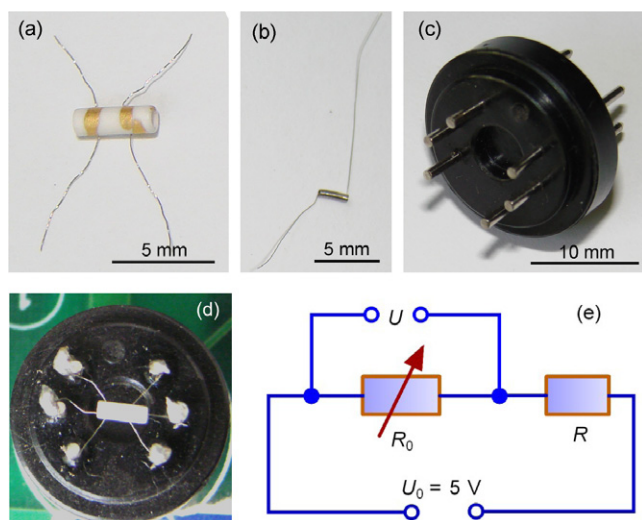
Figure 1. Components of a WO$_3$ sensor and its gas-sensing testing principle: (a) an Al$_2$O$_3$ microtube with four Pt electrodes; (b) a heating coil; (c) a pedestal with six poles; (d) a photograph of a complete WO$_3$ sensor; (e) an equivalent circuit for the alcohol-sensing testing system.

Figure 2. (a) An XRD pattern and (b) an SEM image of the tungstate-based inorganic–organic hybrid nanobelts obtained in a H$_2$W$_2$O$_7 \cdot x$H$_2$O/n-octylamine/heptane system.

2.4. Alcohol-sensing measurement with WO$_3$ sensors

The alcohol-sensing properties of WO$_3$ sensors were measured using a commercial computer-controlled HW-30A system under a static testing condition. The sensors, integrated in a large circuit board with 32 inlet sites, were encased in a transparent glass chamber with a volume of 13.8 l. The testing system was placed in a ventilating cabinet with a large draught capacity. Various alcohol vapors (e.g., methanol, ethanol, isopropanol and butanol) were used as the target gases for characterizing the sensing performance of the WO$_3$ sensors. Alcohols were sampled using syringe-like samplers with ranges of 1–10 μl. The alcohol concentrations (2–300 ppm) were calculated according to the alcohol densities and the volume of the chamber. The operating temperatures were 260–360 °C, controlled by an electric heating system (applied voltages: 4.2–5.0 V). The relative humidity (RH) of the environment was 35–50%.
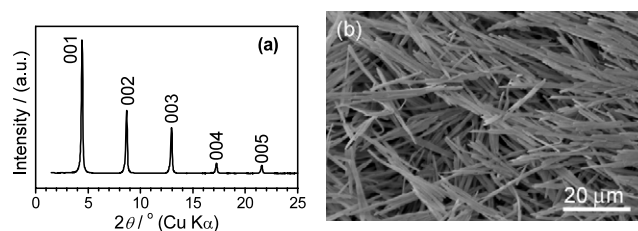
An equivalent circuit of the gas-sensing testing system is given in figure 1(e). As the figure shows, the WO$_3$ sensor (R) is connected in series with a load resistor (R_0) with a known resistance (22–1000 kΩ), and a source voltage (U_0) of 5 V is loaded on the circuit. The system measures the voltages (U) loaded on the resistor R_0, and the resistances (R) of the WO$_3$ sensors can therefore be calculated according to equation (1):

$$R = \frac{U_0 - U}{U} \times R_0. \tag{1}$$

For reducing gases of alcohols and n-type semiconducting WO$_3$ sensors, the sensitivity (S_r) is defined by equation (2), where R_a and R_g are the resistances of the WO$_3$ sensor in air ambient and in alcohol ambient, respectively:

$$S_r = R_a/R_g. \tag{2}$$

The response time (τ_{res}) is defined as a duration in which the variation amplitude of the voltage of the load resistor is not larger than 5%, starting from the time point of 'gas on'. Similarly, the recovery time (τ_{rec}) is defined as a duration in which the variation amplitude of the voltage of the load resistor is not larger than 5%, starting from the time point of 'gas off'.

3. Results and discussion

3.1. Synthesis and characterization of WO$_3$ nanoplates

WO$_3$ nanoplates were synthesized through a process combining intercalation chemistry with topochemical conversion using H$_2$W$_2$O$_7 \cdot x$H$_2$O as the tungsten source [54]. The intercalation–decomposition–reorganization reactions lead to the formation of tungstate-based inorganic–organic hybrid nanobelts in a reverse-emulsion-like H$_2$W$_2$O$_7 \cdot x$H$_2$O/n-octylamine/heptane medium [53]. Figure 2(a) shows a typical XRD pattern of the resulting tungstate-based inorganic–organic hybrid. It is typically characteristic of a highly ordered layered compound, having a series of peaks reflected from (00*l*) crystal planes in the low range of 2θ, with a gradually decreasing intensity. It is close to the literature data that we reported before [53]. The interlayer distance of the above layered compound is calculated to be about 2.5 nm. A typical SEM image (figure 2(b)) indicates that the tungstate-based inorganic–organic hybrid consists of quasi-one-dimensional (1D) nanostructures with a length range of 15–30 μm. The TEM image (not shown) suggests that the quasi-1D nanostructures are nanobelts with a thickness range of 50–80 nm [55].

The tungstate-based inorganic–organic hybrids consist of inorganic [WO$_6$] octahedral layers and organic ammonium layers, and the organic layers can be readily removed using a concentrated HNO$_3$ aqueous solution at room temperature [54]. Platelike H$_2$WO$_4$ nanocrystals are obtained after drying the HNO$_3$-treated product at 120 °C, and the H$_2$WO$_4$ nanoplates have a perfect single-crystalline structure [54]. The crystal water molecules in H$_2$WO$_4$ nanoplates can be readily removed by calcining them at an elevated temperature. Figure 3 shows the typical XRD patterns of the products calcined at various temperatures of 250–500 °C in air for 2 h. They can readily be indexed to a triclinic WO$_3$ phase (space group: $P1$ [1]) according to the JCPDS card No. 32-1395. The refinement of the XRD patterns is performed and the resultant lattice parameters are shown in table 1. One can see that the lattice parameters calculated are very close to the literature data for the triclinic WO$_3$ phase. As figure 3 shows, with increases in calcination

Table 1. Summary of the calculated lattice parameters, cell volumes and crystal sizes of the WO_3 samples obtained at various calcination temperatures according to their corresponding XRD results from figure 3.

Samples	Lattice parameters calculated[a]						Cell volume[a] ($Å^3$)	Crystal size[b] (nm)
	a (Å)	*b* (Å)	*c* (Å)	α (deg)	β (deg)	γ (deg)		
WO_3-250	7.33(2)	7.52(1)	7.68 (2)	88.7(2)	90.8(3)	91.3(3)	424(1)	15.0
WO_3-300	7.33(1)	7.51(1)	7.68 (2)	88.8(2)	91.0(2)	90.8(2)	423(1)	17.8
WO_3-400	7.322(3)	7.521(6)	7.691(3)	88.84(3)	91.1(1)	90.7(1)	423.4(7)	21.4
WO_3-500	7.322(7)	7.522(5)	7.687(8)	88.84(8)	91.1(1)	90.7(1)	423.2(6)	23.7
Triclinic[c] WO_3	7.309	7.522	7.678	88.81	90.92	90.93	421.92	—

[a] Refined in a triclinic system with a UnitCell program (a method developed by T J B Holland and S A T Redfern in 1995), using a wavelength of 1.5406 Å, by minimizing the sum of squares of residuals in 2θ.

[b] Calculated using the Scherrer method ($d = 0.89\lambda/B\cos\theta$) from the positions and linewidths of the 200 reflection.

[c] Data from the JCPDS card No. 32-1395.
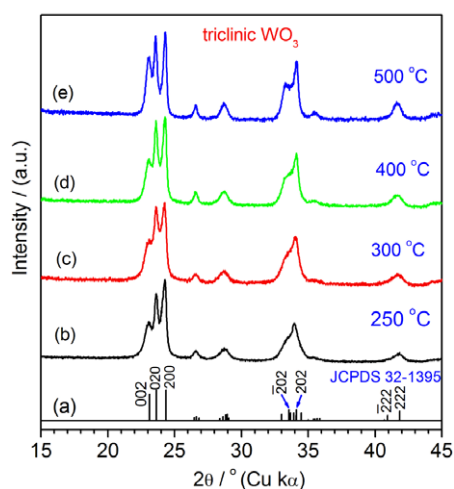
Figure 3. XRD patterns of the WO_3 nanocrystals derived by calcining the HNO_3-treated products (i.e., tungstic acid) at various temperatures in air for 2 h: (a) the standard pattern of triclinic WO_3 (JCPDS No. 32-1395), (b) at 250 °C, (c) at 300 °C, (d) at 400 °C and (e) at 500 °C.

temperatures from 250 to 500 °C, the linewidths of the Bragg lines of the as-obtained WO_3 nanocrystals gradually become keen-edged. The evolution in the linewidths of the Bragg lines probably suggests enhancement in the degree of dehydration and reorganization during the calcination process. An evaluation of the crystal sizes of the WO_3 samples calcined at various temperatures is conducted using the Scherrer method on the basis of the positions and linewidths of the 200 reflection peaks, and the as-obtained results are listed in table 1. The calculated crystal sizes increase from 15.0 to 23.7 nm as the calcination temperature increases from 250 to 500 °C. In fact, the N_2 adsorption–desorption measurement indicates that the specific surface area of the WO_3-250 sample is higher than 200 $m^2 g^{-1}$, and the other WO_3 nanocrystals have specific surface areas larger than 150 $m^2 g^{-1}$ [54].

Figure 4 shows the TEM observations of the WO_3 nanocrystals obtained by calcining H_2WO_4 nanoplates at 250–500 °C in air. Figure 4(a) shows a low magnification TEM image of WO_3-250, which presents a quadrangular platelike morphology with a side length of 300–500 nm. Judging from the contrast of the TEM image, one can find that these

WO_3 nanoplates have a very low thickness. Besides the nanoplatelike shape, one can also find some one-dimensional nanostructures (figure 4(a), marked with an arrow), which are probably tubular structures coiling from the thin WO_3 nanoplates. Figure 4(b) shows a typical high resolution TEM (HRTEM) image of an individual WO_3 nanoplate, and the clear crystal lattices indicate that the WO_3 nanoplate is of a single-crystalline structure. The distances of the two-dimensional crystal lattices are 0.376 nm and 0.364 nm, which can be indexed to (020) and (200) planes of triclinic WO_3, respectively. Figure 4(c) shows the corresponding FFT pattern of figure 4(b), and the ordered reflecting spots corroborate that the as-obtained WO_3 nanoplate is a single-crystalline one. Figure 4(d) shows a typical TEM image of the sample of WO_3-300, and it consists of WO_3 nanoplates, close to the case for WO_3-250. A TEM image of sample WO_3-400 is shown in figure 4(e). It also takes on a platelike morphology. An HRTEM image (figure 4(f)) and its corresponding FFT pattern indicate that the WO_3 nanoplates obtained at 400 °C are single-crystalline ones, similar to those obtained at 250 °C. The two-dimensional interplanar spacings from the HETEM image can be determined as 0.376 nm and 0.365 nm, related to the (020) and (200) planes, respectively. The angle between the [200] and [020] directions is about 91°, very close to the γ value of the triclinic WO_3 phase. Figure 4(g) shows a TEM image of the sample WO_3-500, and figure 4(h) shows its HRTEM image, which indicates that the interplanar spacing is $\sim$0.364 nm, relating to the (200) plane. The interplanar distances of the (010) and (100) planes are double the values for the (020) and (200) planes, i.e., $\sim$0.752 nm and $\sim$0.728 nm, respectively. The results are very close to the values of *a* and *b* determined by the XRD analysis (table 1), which corroborates the as-obtained samples being triclinic WO_3 phases.

One can find that the platelike morphology is still maintained, but the sharp angles of the nanoplates (figure 4(a)) gradually become rounder and rounder as the calcining temperature increases from 250 to 500 °C, as shown in figures 4(a), (c), (e), (g). The above result suggests that crystal growth and atom rearrangement occur at the sharp edges due to their high energy levels when calcining the samples at an elevated temperature. But the platelike shape of the WO_3 nanocrystals is retained, because the voids between the nanoplates block the transfer of atoms and then inhibit the
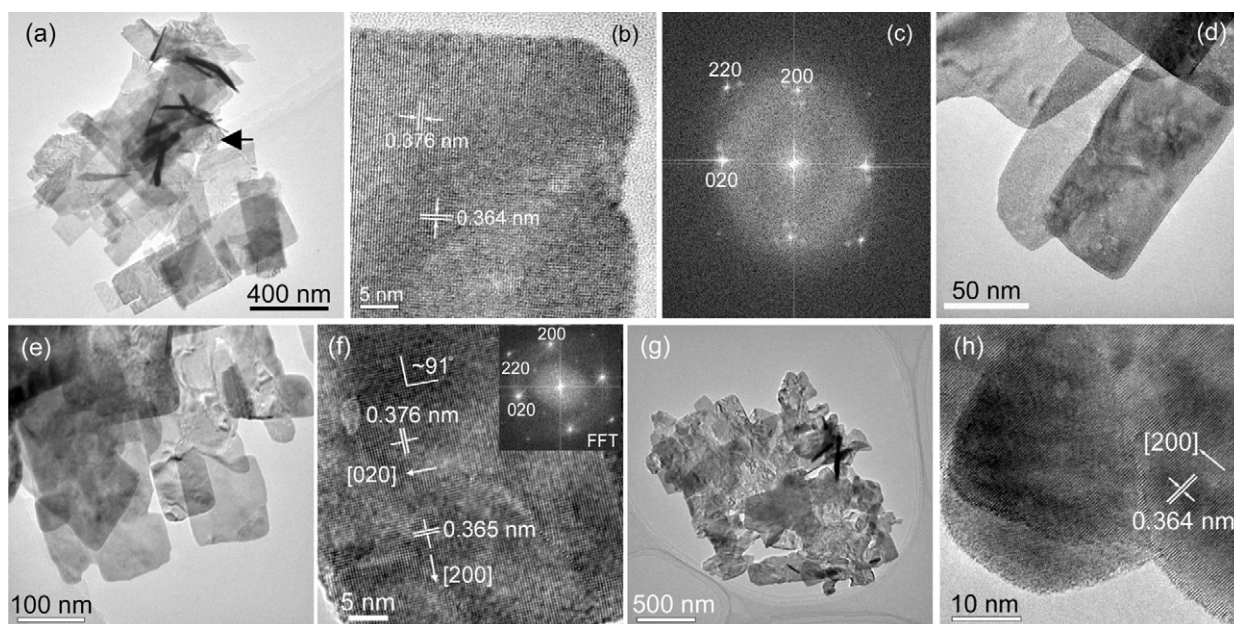
Figure 4. (a) A TEM image, (b) an HRTEM image and (c) its FFT pattern for WO₃ nanoplates calcined at 250 °C; (d) a TEM image of WO₃ nanoplates calcined at 300 °C; (e) a TEM image and (f) an HRTEM image of WO₃ nanoplates calcined at 400 °C (the inlet in f is the FFT pattern); (g) a TEM image and (h) an HRTEM image of WO₃ nanoplates calcined at 500 °C.

growth of WO₃ nanoplates even at an elevated temperature up to 500 °C. The platelike shape is very helpful for improving the gas-sensing performance of the as-obtained WO₃ sensors. It is noteworthy that the degree of order of the lattices is obviously improved when the calcination temperature increases from 250 to 500 °C, judging from the HRTEM images (figures 4(b), (f), (h)). This result is in agreement with the evolution of the XRD patterns (figure 3).

3.2. The alcohol-sensing response of WO₃ nanoplate sensors

First of all, we use the sample of WO₃-250 as the active element for evaluating the alcohol-sensing properties of single-crystalline WO₃ nanoplates. Figure 5 shows the response (U–t) plots recorded for an operating temperature of 300 °C with various concentrations of alcohols, including methanol (10–300 ppm; figure 5(a)), ethanol (10–200 ppm; figure 5(b)), isopropanol (10–200 ppm; figure 5(c)) and butanol (2–100 ppm; figure 5(d)). As figure 5 shows, the voltages (U) of the known resistor in air are very low (0.1–0.2 V), indicating that the resistances of the WO₃ nanoplate sensors in air are very high, due to the source voltage being kept constant at 5 V, as shown in figure 1(e). Upon exposure to alcohols, the voltages (U) of the known resistor increase sharply up to 1–3 V, whereas the voltages (U) are returned to their initial levels when the alcohol vapors are removed, as shown in figure 5, indicating that the resistances of the WO₃ nanoplate sensors decrease remarkably in alcohol vapors. The values of U increase with the increases in the concentrations of the alcohols, which is similar to the literature findings [17, 20]. One can also see that the response rate of butanol is obviously slower than that of methanol, ethanol or isopropanol. The above phenomena may be attributed to the slow evaporation rate of butanol, because of
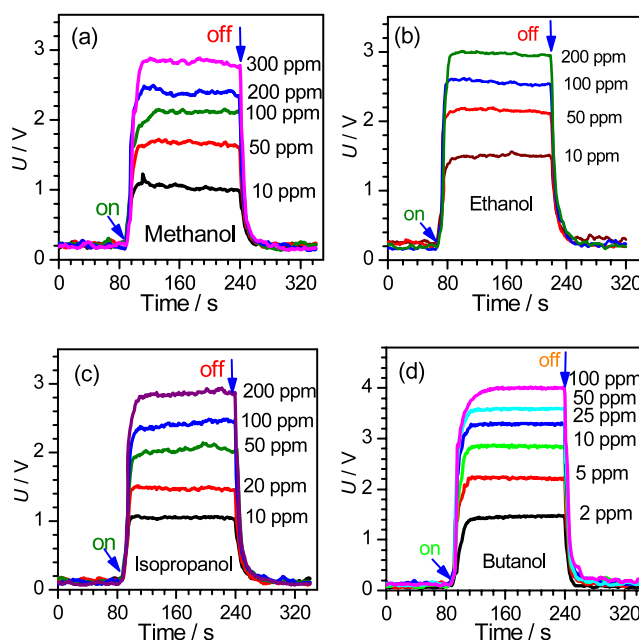
Figure 5. Alcohol-sensing response characteristics of the WO₃-250 nanoplate sensors for an operating temperature of 300 °C: (a) methanol, (b) ethanol, (c) isopropanol and (d) butanol with various concentrations.

the long carbon chain, when compared with methanol, ethanol and isopropanol.

According to the equivalent circuit of the gas-sensing testing system (figure 1(e)), the resistance (R) of the WO₃ nanoplate sensor in air (R_a) and in alcohol vapors (R_g) can be calculated using equation (1). Under the present testing conditions, U_0 is 5 V, R_0 is 47 kΩ for figures 5(a), (c), (d)
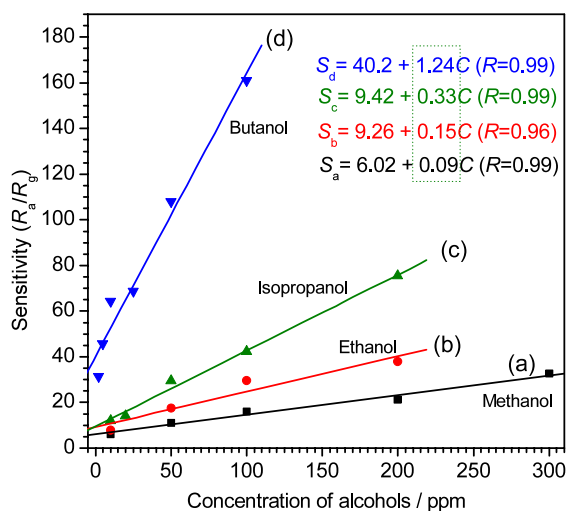
Figure 6. Sensitivities (R_a/R_g) of the WO$_3$-250 nanoplate sensors as a function of alcohol concentration with an operating temperature of 300 °C: (a) methanol, (b) ethanol, (c) isopropanol and (d) butanol.

Figure 7. Response and recovery times of the WO$_3$-250 nanoplate sensors operating at 300 °C under various alcohol concentrations: (a) methanol, (b) ethanol, (c) isopropanol and (d) butanol.

or 22 kΩ for figure 5(b), and the U values are obtained from the response plots (figure 5). The sensitivities of the WO$_3$ nanoplate sensors, defined by equation (2), are therefore determined.

Figure 6 shows the changing trend of the sensitivities of WO$_3$-250 nanoplate sensors as the concentrations of alcohols increase from several ppm to several hundred ppm at an operating temperature of 300 °C. One can find that the sensitivities increase with increase in the concentrations of the alcohols, including methanol, ethanol, isopropanol and butanol. For methanol, the sensitivity increases from 6 at 10 ppm to 33 at 300 ppm, as shown in figure 6(a). As figure 6(b) shows, the sensitivity for ethanol increases from 8 at 10 ppm to 38 at 200 ppm. For the case of isopropanol, the sensitivity increases from 12 to 75 as its concentration increases from 10 to 200 ppm, as shown in figure 6(c). The sensitivity of WO$_3$ nanoplate sensors to butanol increases from 31 at 2 ppm to 161 at 100 ppm (figure 6(d)), much higher than the sensitivities to methanol, ethanol or isopropanol. Another interesting phenomenon is that there is a linear relationship between the sensitivity and the concentration for all the test alcohols. The solid lines in figure 6 are the linear fitting results and their linear correlation coefficients (R) are not less than 0.96. On comparing the slope coefficients of the fitting equations (insets in figure 6), one can see that the rate of increase in the sensitivity to butanol (1.24 per ppm) is much higher than those in the sensitivities to isopropanol (0.33 per ppm) and ethanol (0.15 per ppm), whereas the sensitivity to methanol shows the lowest rate of increase (0.09 per ppm).

Besides the sensitivity, the response and recovery times are also important parameters for the evaluation of a chemical sensor. Figure 7 shows the response and recovery times of the WO$_3$-250 nanoplate sensors upon exposure to various alcohol vapors with different concentration levels at an operating temperature of 300 °C. As figure 7(a) shows, the response times of methanol are close to their recovery times for a concentration range of 10–300 ppm, and their values are about
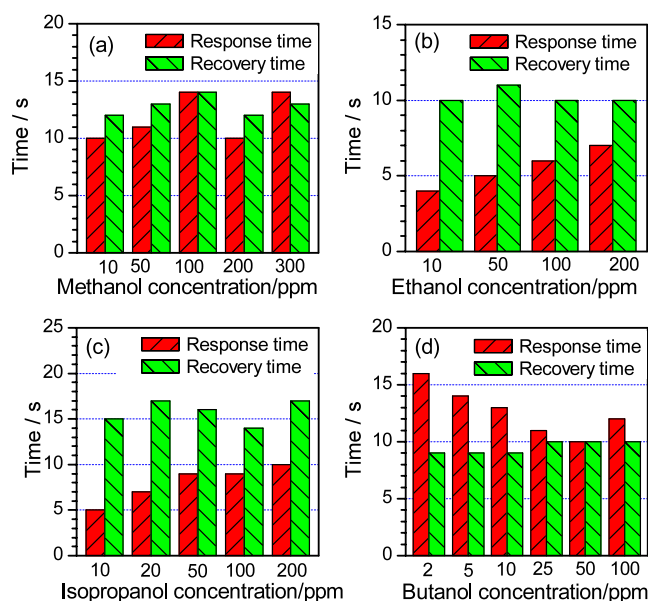
10–14 s. For ethanol, as shown in figure 7(b), the response times are less than 7 s for the concentration range of 10–200 ppm, but their recovery times are about 10 s, longer than their corresponding response times. The response and recovery times of isopropanol are shown in figure 7(c). One can see that the response time (less than 10 s) is obviously shorter than the corresponding recovery time (about 15 s). But for the case of butanol, the response time (10–15 s) is longer than the corresponding recovery time (9–10 s), especially in the low concentration range of 2–10 ppm, as shown in figure 7(d). This is very different from the cases for methanol, ethanol and isopropanol, which have longer recovery times than their corresponding response times. The above-mentioned difference suggests that the semiconductor time response is strongly correlated with the length of alcohol alkyl tails, which have a decreasing vapor tension from methanol to butanol. The lower volatility of butanol with a longer alkyl tail probably accounts for the above-mentioned difference. Similar results were observed for V$_2$O$_5$ ribbon sensors [26a].

3.3. Effects of calcining and operating temperatures

Figure 8 compares the ethanol response performance of the sensors with WO$_3$ nanoplates, which are obtained by calcining H$_2$WO$_4$ nanoplates at various temperatures (e.g., 250, 300, 400 and 500 °C). The operating temperatures for the WO$_3$ sensors vary from 260, 300 to 360 °C, and the concentrations of the ethanol vapors vary from 10 to 300 ppm. As figure 8 shows, all the WO$_3$ nanoplate sensors calcined at various temperatures show unique ethanol-sensing properties at various operating temperatures of 260–360 °C. On comparing the response curves vertically in figure 8, one can see that the higher the calcining temperatures for the synthesis of WO$_3$ nanoplates are, the sharper the response curves are upon exposure to
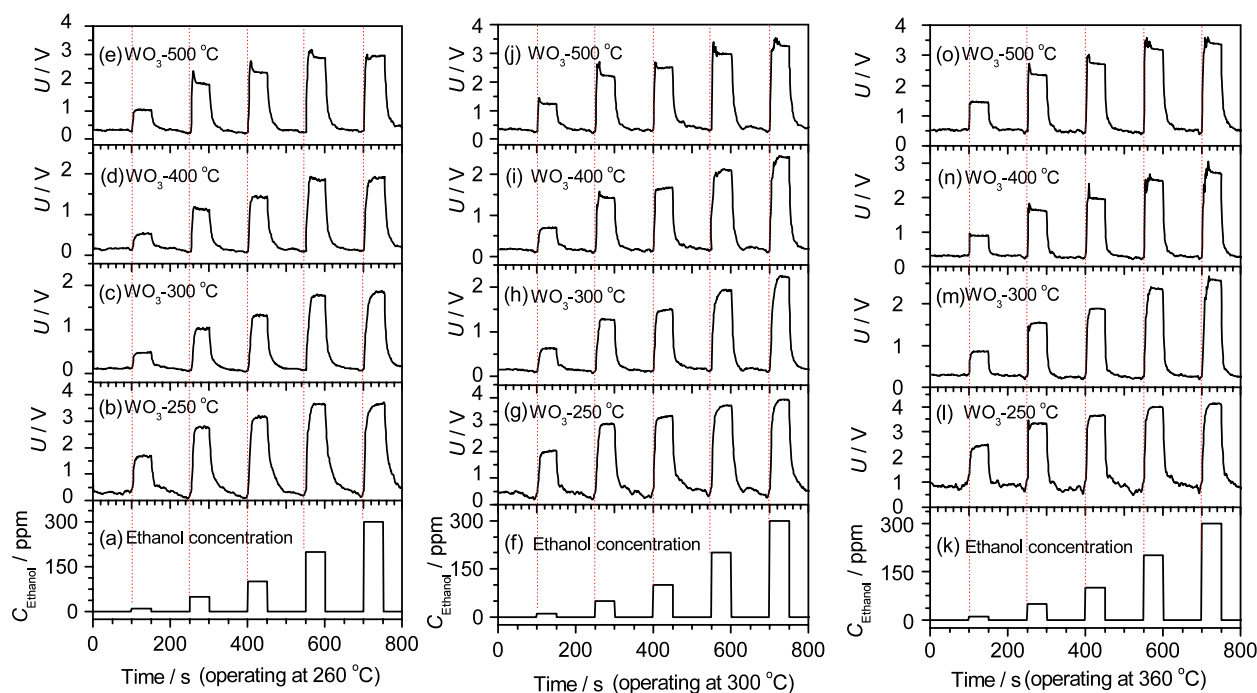
Figure 8. Ethanol response plots of the sensors with WO$_3$ nanoplates calcined at various temperatures and with different operating temperatures of ((b)–(e)) 260 °C, ((g)–(j)) 300 °C and ((l)–(o)) 360 °C, $R_0 = 47$ kΩ, $U_0 = 5$ V. The plots in (a), (f) and (k) show the ethanol concentrations varying with the testing time.

(or discharging) ethanol vapors (figures 8(b)–(e), figures 8(g)–(j) and (l)–(o)). On comparing them horizontally, one can readily see that the higher the operating temperatures are, the sharper the response curves are (figures 8(b), (g) and (l) for WO$_3$-250, figures 8(c), (h) and (m) for WO$_3$-300, figures 8(d), (i) and (n) for WO$_3$-400, and figures 8(e), (f) and (o) for WO$_3$-500). Figure 9 shows the changing trend in the sensitivities of the WO$_3$ nanoplate sensors for 100 ppm ethanol vapors at various operating and calcining temperatures. The sensitivities increase with the decreases in operating temperatures. The sensitivity is higher than 35 at an operating temperature of 260 °C (figure 9(a)), whereas the sensitivities at 360 °C decrease to a range of 18–20 (figure 9(c)). The change of the sensitivities with the operating temperatures for the WO$_3$ nanoplate sensors is different from the cases for ZnO nanowire sensors and ZnO nanoplate sensors, in which their sensitivities increase with the operating temperatures [17b, 19]. For the sensors consisting of WO$_3$ nanoplates calcined at various temperatures (250–500 °C), their sensitivities do not fluctuate very much, especially at high operating temperatures (e.g., 300 and 360 °C), as shown in figures 9(b) and (c).

Figure 10 shows the change in the response times of the WO$_3$ nanoplate sensors when exposed to 100 ppm ethanol vapors at various operating and calcining temperatures. As figure 10 shows, the response times decrease obviously with increases in the operating temperature. For the WO$_3$-250 and WO$_3$-300 sensors, the response times are 9, 7 and 6 s, operated at 260, 300 and 360 °C, respectively. For the WO$_3$-400 and WO$_3$-500 sensors, the response times are 6, 5 and 4 s, operated at 260, 300 and 360 °C, respectively. The response times also decrease when the calcining temperatures of the
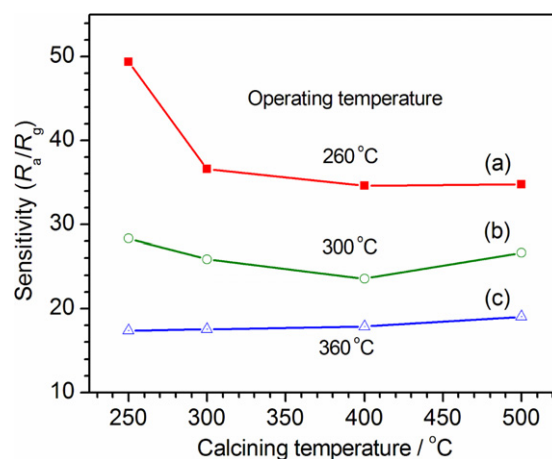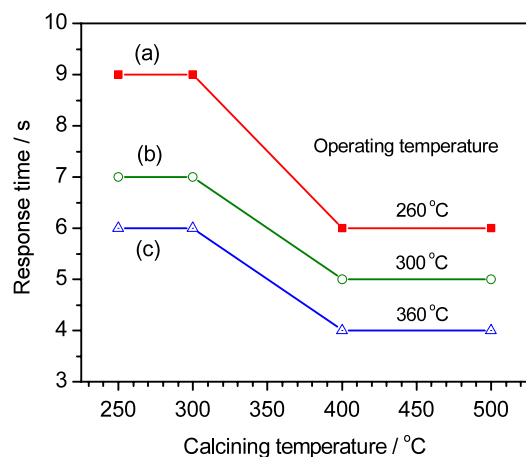

Figure 9. Change in the sensitivities of the WO$_3$ nanoplate sensors to 100 ppm ethanol vapors at various operating and calcining temperatures.

WO$_3$ nanoplates increase. The response times of WO$_3$-250 and WO$_3$-300 sensors are 9 s, whereas it is 6 s for WO$_3$-400 and WO$_3$-500 sensors at an operating temperature of 260 °C, as shown in figure 10(a). At a high operating temperature of 360 °C, the response times decrease from 6 s for WO$_3$-250 and WO$_3$-300 sensors to 4 s for WO$_3$-400 and WO$_3$-500 sensors (figure 10(d)).

Comprehensively considering the ethanol-sensing results of figures 8–10, one can see that the high calcining temperatures of the WO$_3$ nanoplates have no apparent effect on the sensitivity of the as-obtained WO$_3$ nanoplate sensors,
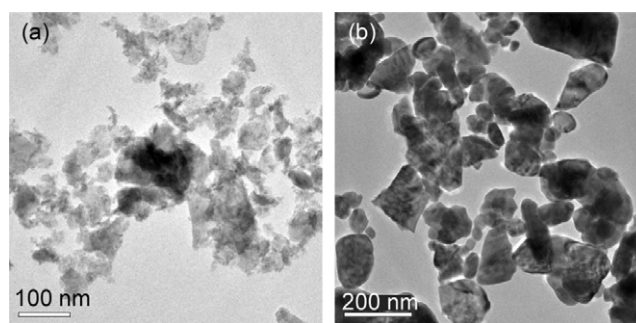
Figure 10. Change in the time of response of WO_3 nanoplate sensors to 100 ppm ethanol vapors at various operating and calcining temperatures.

Figure 11. TEM images of (a) commercial H_2WO_4 powders and (b) the resultant WO_3 nanocrystals obtained by calcining commercial H_2WO_4 powders at 550 °C for 2 h.

Figure 12. Alcohol response plots of the WO_3 nanoparticle sensors at an operating temperature of 300 °C, $R_0 = 470$ kΩ, $U_0 = 5$ V: (a) methanol, (b) ethanol, (c) isopropanol and (d) butanol.

but accelerate the response speeds. On correlating the above results, the XRD analysis in figure 3 and table 1, and the HRTEM observations (figures 4(b), (f), (h)) we can infer that the elevated calcining temperature does not make the sizes of WO_3 nanoplates change obviously, but enhances their crystallinity and reduces the surface crystal defects, which is helpful for speeding up the adsorption, desorption and diffusing process for ethanol vapors on the surfaces of the WO_3 nanoplates.

### 3.4. Effects of sizes and morphologies of WO₃ nanocrystals

To demonstrate the effect of particle sizes and morphology on the alcohol-sensing response of WO_3 nanocrystal sensors, we calcined commercial H_2WO_4 nanocrystals to synthesize WO_3 nanocrystals. Figure 11(a) shows a TEM image of the commercial H_2WO_4 powders. As figure 11(a) shows, the commercial H_2WO_4 powders mainly consist of nanoparticles with sizes of 10–50 nm, and some platelike particles with diameters of 100 nm can also be found. Figure 11(b) shows a TEM image of the as-obtained WO_3 nanocrystals calcined at 550 °C for 2 h. They are not homogeneous in particle size and have a wide size range from 10 to 300 nm. Judging from the contrast of the particles in the TEM image, one can infer that some large particles are probably platelike, but their thicknesses are larger than those of the WO_3 nanoplates derived from the tungstate-based inorganic–organic hybrid nanobelts (figure 4).

The WO_3 nanoparticles derived from the commercial H_2WO_4 were also used to fabricate sensors under similar conditions. Figure 12 shows the typical response of the WO_3 nanoparticle sensors upon exposure to methanol (figure 12(a)), ethanol (figure 12(b)), isopropanol (figure 12(c)) and butanol (figure 12(d)), with various alcohol concentrations at an operating temperature of 300 °C. One can find that the change (ΔU) in voltage on exposure to air and to alcohol vapors is 0.2–1.0 V, smaller than that ($\Delta U \sim 1$–3 V) for the WO_3 nanoplate sensors, as shown in figure 5, indicating that the WO_3 nanoparticle sensors have a greater resistance than the
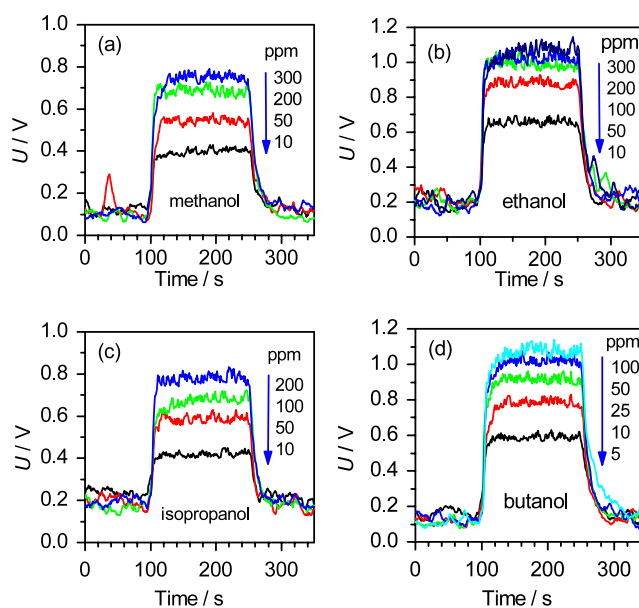
WO_3 nanoplate sensors. Furthermore, the WO_3 nanoparticle sensors are not stable in alcohol-sensing response, and show zigzags in their U–t plots.

The sensitivities of the WO_3 nanoparticle sensors are shown in figure 13. As figure 13 shows, the sensitivities of the WO_3 nanoparticle sensors are lower by one order of magnitude than those of the WO_3 nanoplate sensors (figure 6) for the cases of isopropanol and butanol vapors. The sensitivities of the WO_3 nanoparticle sensors to isopropanol vapors with a concentration range of 10–200 ppm are less than 5, whereas they are up to 75 for the WO_3-250 nanoplate sensors for 200 ppm isopropanol vapor (figure 6(c)). The sensitivities of the WO_3 nanoparticle sensors to butanol vapors (5–100 ppm) are less than 15, while the sensitivity of the WO_3-250 nanoplate sensors can be as high as 160 for a 100 ppm butanol vapor (figure 6(d)). For methanol and ethanol vapors (10–300 ppm), the sensitivities of the WO_3 nanoparticle sensors are less than 9 and 8, respectively, which are very much lower than those of the WO_3-250 nanoplate sensors, as shown in
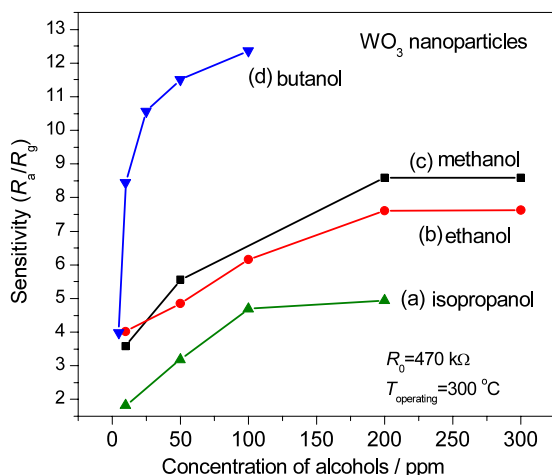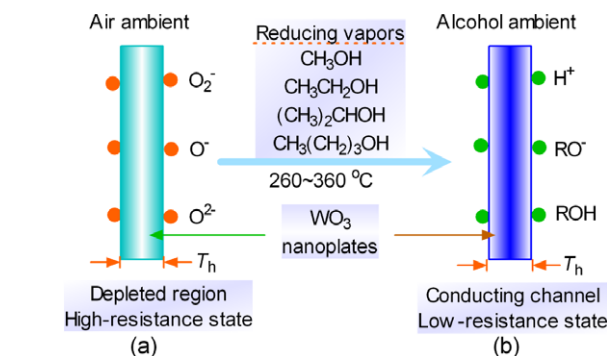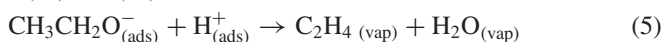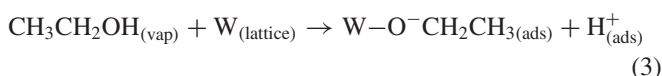
Figure 13. Comparison of the sensitivities of the WO$_3$ nanoparticle sensors to alcohol vapors at an operating temperature of 300 °C: (a) isopropanol, (b) ethanol, (c) methanol and (d) butanol.

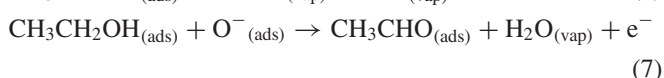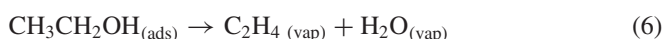**Figure 14.** A schematic representation of the alcohol-sensing mechanism for WO$_3$ nanoplate sensors.

figures 6(a) and (b). In addition, the sensitivities of the WO$_3$ nanoparticle sensors also increase with the increases in the alcohol concentrations, but the linear relationship between the sensitivities and alcohol vapor concentrations does not occur for the WO$_3$ nanoparticle sensors. The low sensitivities and the non-linear sensitivity–concentration relationship can be attributed to the large sizes and non-uniform shapes of the WO$_3$ nanoparticles used.

3.5. Mechanisms for alcohol sensing for WO$_3$ sensors

The space-charge layer model has often been applied to explain possible gas-sensing mechanisms of a semiconducting metal oxide sensor [9, 14, 17]. WO$_3$ is a typical n-type metal oxide semiconductor, and the space-charge layer model is appropriate for WO$_3$ sensors. When a WO$_3$ nanoplate sensor is exposed to air, O$_2$ molecules will adsorb on the surfaces of WO$_3$ nanoplates. The O$_2$ molecules adsorbed then transform to oxygen ions (e.g., O$^-$, O^{2-}, or O$_2^-$) by capturing free electrons from the conductance band of WO$_3$ nanoplates [56]. The electron-capture process leads to a depletion region in WO$_3$ nanoplates, which reduces the conductive regions of WO$_3$ nanoplates, and thus a high resistance state is formed, as shown in figure 14(a). When the WO$_3$ nanoplate sensors are exposed to alcohol vapors (reducing gases), the alcohol molecules adsorbed on the surfaces of the WO$_3$ nanoplates can provide electrons to reduce oxygen ions, and then release free electrons back into the WO$_3$ nanoplates. The above process decreases the depletion region of the WO$_3$ nanoplates and forms a conducting channel, which results in a low resistance state, as shown in figure 14(b). Taking ethanol as the example, the possible reactions can be expressed using equations (3)–(8) [17, 41, 56, 57]:

$$CH_3CH_2OH_{(vap)} + W_{(lattice)} \rightarrow W-O^-CH_2CH_{3(ads)} + H^+_{(ads)} \tag{3}$$

$$H^+_{(ads)} + O^-_{(ads)} \rightarrow H_2O_{(vap)} \tag{4}$$

$$CH_3CH_2O^-_{(ads)} + H^+_{(ads)} \rightarrow C_2H_{4\ (vap)} + H_2O_{(vap)} \tag{5}$$

$$CH_3CH_2OH_{(ads)} \rightarrow C_2H_{4\ (vap)} + H_2O_{(vap)} \tag{6}$$

$$CH_3CH_2OH_{(ads)} + O^-_{(ads)} \rightarrow CH_3CHO_{(ads)} + H_2O_{(vap)} + e^- \tag{7}$$

$$CH_3CHO_{(ads)} + O^-_{(ads)} \rightarrow CH_3COOH_{(vap)} + e^-. \tag{8}$$

Ethanol molecules are adsorbed on the surface tungsten atoms of WO$_3$ via the oxygen atoms of the hydroxyl groups (equation (3)), and the resultant H$^+$ ions react with O$^-$ ions to form water molecules which are then desorbed (equation (4)). At the elevated temperatures (200–500 °C), the adsorbed ethanol molecules and ethoxy groups can be decomposed into ethylene and water that are then desorbed (equations (5) and (6)). The ethanol adsorbed can also be decomposed to acetaldehyde that then turns into a vapor of acetic acid, desorbed from the surfaces of WO$_3$, as shown in equations (7) and (8). The difference in ionic character of the –OH group and its associated acidity for various alcohols can account for the difference in the gas-sensing responses (i.e., sensitivities and response speeds) [26].

The sizes and shapes of the semiconductor nanocrystals, together with their configuration, are the key factors influencing the gas-sensing properties [6, 14]. One of the primary strategies for enhancing the gas-sensing performance is to reduce the sizes of the active materials down to several nanometers. However, the particles with nanoscale sizes tend to form aggregates with large secondary sizes due to the van der Waals attraction, as shown in figure 15(b). The long diffusion length and the sluggish diffusion of a target gas into the inner parts of the secondary aggregates make this an inefficient way to improve the gas-sensing property. Only the resistance of the primary nanoparticles near the surfaces of the aggregates is affected by the target gas molecules, and thus the sensitivity is low and the response time is long, as shown in figure 15(d). But for the ultrathin 2D nanoplates, they are usually draped to form a loose assembly containing a great number of gaps due to the steric effect of the platelike morphology, as shown in figure 15(a). The gaps between nanoplates not only enhance the effective surface for adsorbing target gases, but also provide capacious channels for target gases to diffuse in [6]. The large surface areas for the effective adsorption and the loosely assembled structures allowing the rapid diffusion of target gases are helpful for enhancing the
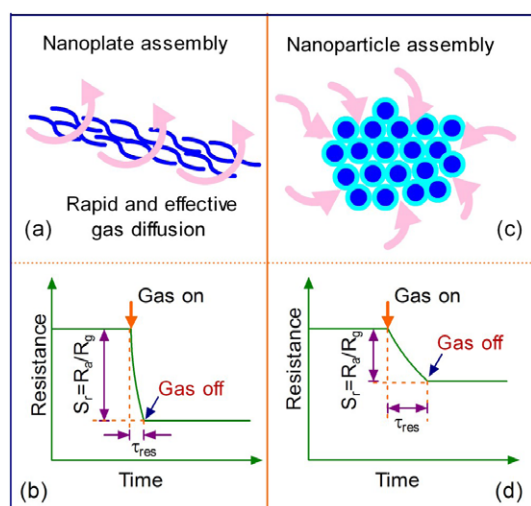
Figure 15. A schematic representation of the configuration effect of the WO₃ nanoplates and nanoparticles on the alcohol-sensing performance.

sensitivities and shortening the response times of the 2D nanoplate sensors (figure 15(b)) [6].

In this work, the WO₃ nanoplates are derived from an intercalated intermediate precursor, and the thicknesses of the primary sheets should be ultralow: down to several nanometers. This thickness (T_h) of WO₃ nanoplates is comparable with that of the electron depletion layer (L_d), and thus a complete depletion can be formed in a WO₃ nanoplate sensor when exposed to an air ambient and $T_h < 2L_d$ [6, 20]. The achievement of a complete depletion may account for the linear relationship between the sensitivities and alcohol concentrations for the WO₃ nanoplate sensors (figure 6) [20]. For WO₃ nanoparticle sensors, the relationship between the sensitivities and the alcohol concentrations is obviously deflected from a straight line, as shown in figure 13. A linear relationship between the sensitivity and ethanol vapor concentrations was also observed for SnO₂ nanowire and nanorod sensors, and the authors attributed the linear dependence to the small size effect and the special crystalline surfaces exposed [16]. Therefore, the linear dependence for WO₃ nanoplate sensors can also be attributed to their small thicknesses and platelike morphologies.

Actually, the sensitivity of a semiconducting oxide gas sensitive sensor can be empirically described using equation (9) [58]:

$$S_r = a + bC_g^N. \qquad (9)$$

Here, S_r is the sensitivity, C_g is the concentration of target gases, and a, b are constants. The exponent N depends on the charge of the surface species, the stoichiometry of the elementary reactions on the surface, and the size and morphology of the active sensing materials [17b, 20]. N has some rational fraction values, e.g., 1 or 1/2. As figures 6 and 13 show, N is 1 for the WO₃ nanoplate sensors and near to 1/2 for the WO₃ nanoparticle sensors in the test alcohol concentration range of 2–300 ppm.

3.6. Comparison of WO₃ nanoplate sensors with other sensors

The alcohol-sensing properties of the WO₃ nanoplate sensors are better than or comparable to those of the sensors with other oxide semiconductors. Zhan *et al* [19] reported an ethanol-sensing sensor based on porous ZnO nanoplates with thicknesses of about 19 nm, having a maximum sensitivity of 8.9 at 380 °C, and having response and recovery times of 32 and 17 s for a 100 ppm ethanol vapor, respectively. Xu *et al* [57] reported on a series of metal-doped ZnO sensors and found that the Ru-doped ZnO sensor had the highest sensitivity of 18 for a 50 ppm ethanol vapor at 350 °C. Chen *et al* [20] reported a ZnO nanotube sensor with sensitivities of 2.6–59.3 for 1–500 ppm ethanol vapors at 300 °C. Wang *et al* [18] reported an aligned ZnO nanorod sensor with a high sensitivity of ∼100 for a 100 ppm ethanol vapor at 300 °C, but its response and recovery times were longer than those of the present WO₃ nanoplate sensors. Wang *et al* [17] reported a series of ethanol-sensing sensors based on SnO₂, ITO and ZnSnO₃ nanowires, whose sensitivities ranged in 20–40 for 100–500 ppm ethanol vapors operating at 300–400 °C. Kruis *et al* [59] investigated the ethanol response of Ag-modified SnO₁.₈ nanoparticle sensors, finding that Ag nanoparticle (5 nm, 0.1–5.0%) can speed up the response, but the recovery time is still longer than ∼50 s at 400 °C for a 1000 ppm ethanol vapor. Galvagno *et al* [60] reported CeO₂-doped Fe₂O₃ nanoparticle films used for methanol sensors, but the sensitivity is less than 10 at 400 °C for 100–500 ppm methanol vapors. Li *et al* [14] reported a hydrothermal synthesis of V₂O₅ nanobelts and investigated their ethanol-sensing performance. However, its sensitivity at 200 °C is less than 5, and its response and recovery times are as long as 30–50 s. Wu *et al* [62] reported a room temperature ethanol sensor based on an m-CNT/NaClO₄/Ppy blended material, but its sensitivity is lower than 1.5 and its response times are also very long (e.g., 20 s) for a 30 000 ppm ethanol vapor. Wang *et al* [63] reported flute-like porous α-Fe₂O₃ nanorods and branched nanostructures, which showed unique ethanol-sensing performance with sensitivities of 15–90, response times of 1–4 s and recovery times of 4–8 s, but such α-Fe₂O₃ nanorods are difficult to produce on a large scale. The WO₃ nanoplate sensors obtained in this work have a sensitivity of 50 for a 100 ppm ethanol vapor at 260 °C, and have a high sensitivity of 160 for a 100 ppm butanol vapor at 300 °C.

The WO₃ nanoplate sensors also have better alcohol-sensing properties than the WO₃-based sensors reported in the literature. Aguir *et al* [41] investigated the ethanol-sensing property of bare WO₃ and Au/WO₃ films, and found that Au was a good sensing activator for the WO₃ films as regards ethanol vapors. Solis *et al* [42] reported the ethanol/butanol-sensing property of WO₃ and WO₃–CuWO₄ films. The WO₃ films showed sensitivities of less than 15 for ethanol vapors and 8–25 for butanol vapors in a concentration range of 10–150 ppm operating at 400 °C, and small amounts (less than 10 at.%) of CuWO₄ enhanced their sensitivities to 34 and 50 for ethanol and butanol vapors, respectively, at a low concentration of 5 ppm. Li *et al* [45] synthesized hollow WO₃ spheres templated by carbon microspheres, but the as-obtained WO₃ hollow sphere sensors showed low sensitivities (2–12 for
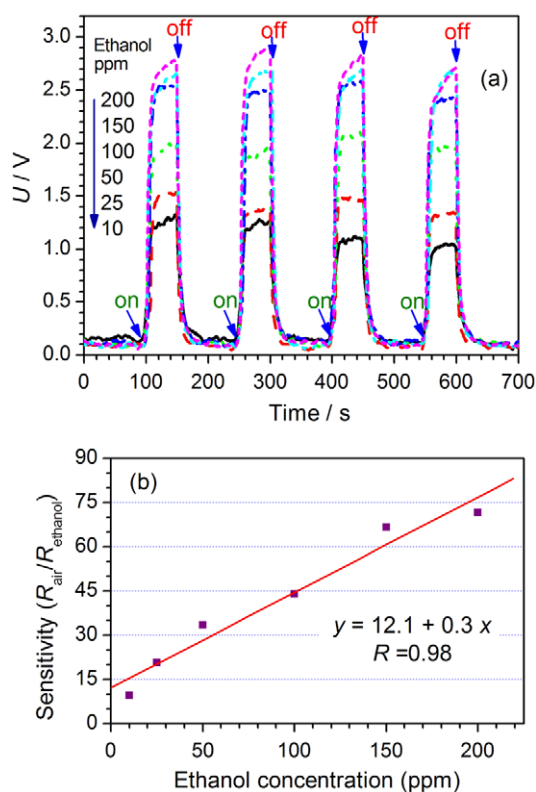
Figure 16. (a) The high stability and (b) sensitivity of the WO$_3$ nanoplate sensors for ethanol vapors when operating at 300 °C with $R_0 = 47$ kΩ and $U_0 = 5$ V.

50–5000 ppm ethanol vapors at 400 °C). But the present WO$_3$ nanoplate sensors without any activators have a high stability and sensitivity to ethanol vapors, as shown in figure 16. The WO$_3$ nanoplate sensors have a good repeatability (figure 16(a)) and a high sensitivity of 10–70 to 10–200 ppm ethanol vapors when operating at 300 °C (figure 16(b)).

4. Conclusions

Single-crystalline 2D WO$_3$ nanoplates have been synthesized via a topochemical transformation process using tungstate-based inorganic–organic hybrid micro/nanobelts as the precursors. The as-obtained WO$_3$ nanoplates with ultrathin thicknesses and high surface areas can be well redispersed in H$_2$O to form a stable WO$_3$ paste, which is then brush-coated onto the surfaces of Al$_2$O$_3$ microtubes to fabricate gas-sensing devices. The as-obtained gas sensors based on the as-synthesized WO$_3$ nanoplates show high sensitivities, rapid response and high stability for alcohol vapors at moderate operating temperatures (260–360 °C). The sensitivity for ethanol increases from 8 at 10 ppm to 38 at 200 ppm, the sensitivity for isopropanol increases from 12 to 75 as their concentrations increase from 10 to 200 ppm, and the sensitivity for butanol increases from 31 at 2 ppm to 161 at 100 ppm. The response and recovery times of methanol are in the range 10–14 s. The response times of ethanol are less than 7 s. The response times of isopropanol are less than 10 s, shorter than its corresponding recovery times (about

15 s), whereas for butanol, its response times (10–15 s) are longer than its corresponding recovery times (9–10 s). The sensitivities of the WO$_3$ nanoplate sensors show a good linear dependence on the alcohol concentrations, which disappears for the WO$_3$ nanoparticle sensors. No obvious effects of the calcining temperatures of WO$_3$ nanoplates on the sensitivity are observed at high operating temperatures (e.g., 300–360 °C), but the response times decrease by 1–2 s when their calcining temperatures increase from 300 to 400 °C. The overall alcohol-sensing performances of the WO$_3$ nanoplate sensors are better than those of most of the oxide semiconductor sensors already developed. The enhanced alcohol-sensing performance can be attributed to the ultrathin platelike morphology, the high crystallinity and the loosely assembled structures of the WO$_3$ nanoplates. The cost-effective synthesis of WO$_3$ nanoplates and their novel applications in alcohol sensing are of great significance in practical nanotechnology.

References

[1] Grundler P (ed) 2007 *Chemical Sensors: An Introduction for Scientists and Engineers* (Berlin: Springer)
[2] Stewart M E, Anderton C R, Thompson L B, Maria J, Gray S K, Rogers J A and Nuzzo R G 2008 *Chem. Rev.* **108** 494–521
[3] Venkatesan B M, Dorvel B, Yemenicioglu S, Watkins N, Petrov I and Bashir R 2009 *Adv. Mater.* **21** 2771–6
[4] Ahn M W, Park K S, Heo J H, Park J G, Kim D W, Choi K J, Lee J H and Hong S H 2008 *Appl. Phys. Lett.* **93** 263103
[5] Kauffman D R and Star A 2008 *Angew. Chem. Int. Edn* **47** 6550–70
[6] Lee J-H 2009 *Sensors Actuators* B **140** 319–36
[7] Franke M E, Koplin T J and Simon U 2006 *Small* **2** 36–50
[8] Patolsky F, Timko B P, Yu G, Fang Y, Greytak A B, Zheng G and Lieber C M 2006 *Science* **313** 1100–4
Patolsky F, Zheng G and Lieber C M 2006 *Anal. Chem.* A **78** 4260–9
[9] Jiang X C and Yu A B 2008 *Langmuir* **24** 4300–9
[10] Kida T, Kurachi H, Yuasa M, Shimanoe K and Yamazoe N 2008 *Adv. Mater. Res.* 1506–9 Hong Kong, P.R.C.
[11] Geng B, Zhan F, Fang C and Yu N 2008 *J. Mater. Chem.* **18** 4977–84
[12] Lu G, Ocola L E and Chen J 2009 *Adv. Mater.* **21** 2487–91
[13] Kim S J, Choi Y M and Lee G W 2008 *Technical Proc. 2008 NSTI Nanotechnology Conf. and Trade Show, 2008 (Quebec City)* pp 97–100
[14] Liu J, Wang X, Peng Q and Li Y 2005 *Adv. Mater.* **17** 764–7
[15] Zhang Y, He X, Li J, Miao Z and Huang F 2008 *Sensors Actuators* B **132** 67–73

[16] Wan Q, Huang J, Xie Z, Wang T H, Dattoli E N and
Lu W 2008 *Appl. Phys. Lett.* **92** 102101
Chen Y J, Nie L, Xue X Y, Wang Y G and Wang T H 2006
Appl. Phys. Lett. **88** 083105

[17a] Xue X Y, Chen Y J, Liu Y G, Shi S L, Wang Y G and
Wang T H 2006 *Appl. Phys. Lett.* **88** 201907

[17b] Wan Q, Li Q H, Chen Y J, Wang T H, He X L, Li J P and
Lin C L 2004 *Appl. Phys. Lett.* **84** 3654

[17c] Xue X Y, Chen Y J, Wang Y G and Wang T H 2005 *Appl.
Phys. Lett.* **86** 233101

[17d] Xue X Y, Chen Y J, Li Q H, Wang C, Wang Y G and
Wang T H 2006 *Appl. Phys. Lett.* **88** 182102

[18] Yang Z, Li L M, Wan Q, Liu Q H and Wang T H 2008 *Sensors
Actuators* B **135** 57–60

[19] Jing Z and Zhan J 2008 *Adv. Mater.* **20** 4547–51

[20] Chen Y J, Zhu C L and Xiao G 2008 *Sensors Actuators*
129 639–42

[21] Teleki A, Bjelobrk N and Pratsinis S E 2008 *Sensors
Actuators* B **130** 449–57

[22] Wang Y, Cao J, Wang S, Guo X, Zhang J, Xia H, Zhang S and
Wu S 2008 *J. Phys. Chem.* C **112** 17804–8

[23] An G, Zhang Y, Liu Z, Miao Z, Han B, Miao S and Li J 2008
Nanotechnology **19** 035504

[24] Zhu H, Gu X, Zuo D, Wang Z, Wang N and Yao K 2008
Nanotechnology **19** 405503

[25] Cao M, Wang Y, Chen T, Antonietti M and
Niederberger M 2008 *Chem. Mater.* **20** 5781–6

[26a] Biette L, Carn F, Maugey M, Achard M F, Maquet J,
Steunou N, Livage J, Serier H and Backov R 2005 *Adv.
Mater.* **17** 2970–4

[26b] Serier H, Achard M F, Babot O, Steunou N, Maquet J,
Livage J, Leroy C M and Backov R 2006 *Adv. Funct.
Mater.* **16** 1745–53

[27] Frank K, Kohler H and Guth U 2008 *Ionics* **14** 363–9

[28] Chen Y J, Zhu C L, Wang L J, Gao P, Cao M S and Shi X L
2009 *Nanotechnology* **20** 045502

[29] Van Hieu N and Duc Chien N 2008 *J. Phys.: Condens. Matter*
403 50–6

[30] He T and Yao J 2007 *J. Mater. Chem.* **17** 4547–57

[31] Zhao Z G and Miyauchi M 2008 *Angew. Chem. Int. Edn*
47 7051–5

[32] Chen D and Ye J 2008 *Adv. Funct. Mater.* **18** 1922–8

[33] Shibuya M and Miyauchi M 2009 *Adv. Mater.* **21** 1373–6

[34] Morales W, Cason M, Aina O, De Tacconi N R and
Rajeshwar K 2008 *J. Am. Chem. Soc.* **130** 6318–9

[35] Wang L, Teleki A, Pratsinis S E and Gouma P I 2008 *Chem.
Mater.* **20** 4794–6

[36] Rossinyol E *et al* 2007 *Adv. Funct. Mater.* **17** 1801–6

[37] Polleux J, Gurlo A, Barsan N, Weimar U, Antonietti M and
Niederberger M 2006 *Angew. Chem. Int. Edn* **45** 261–5

[38] Zhang H X, Yang B Q and Feng P X 2008 *J. Nanomater.* **2008**
1–5

[39] Rout C S, Govindaraj A and Rao C N R 2006 *J. Mater. Chem.*
16 3936–41

[40] Deb B, Desai S, Sumanasekera G U and Sunkara M K 2007
Nanotechnology **18** 285501

[41] Labidi A, Gillet E, Delamare R, Maaref M and Aguir K 2006
Sensors Actuators B **120** 338–45

[42] Damian M A, Rodriguez Y, Solis J L and Estrada W 2003
Thin Solid Films **444** 104–10

[43] Kim Y S *et al* 2005 *Appl. Phys. Lett.* **86** 213105

[44] Rout C S, Kulkarni G U and Rao C N R 2007 *J. Phys. D:
Appl. Phys.* **40** 2777–82

[45] Li X L, Lou T J, Sun X M and Li Y D 2004 *Inorg. Chem.*
43 5442–9

[46] Rout C S, Ganesh K, Govindaraj A and Rao C N 2006 *Appl.
Phys.* A **85** 241–6

[47] Huang S Z, Lin W and Chen W Z 2008 *Advanced Materials
Research* pp 126–8

[48] Siciliano T, Tepore A, Micocci G, Serra A, Manno D and
Filippo E 2008 *Sensors Actuators* B **133** 321–6
Choi Y G, Sakai G, Shimanoe K and Yamazoe N 2004
Sensors Actuators B **101** 107–11

[49] Sauerwald T, Skiera D and Kohl C-D 2007 *Appl. Phys.* A
87 525–9

[50] Rout C S, Hegde M and Rao C N R 2008 *Sensors Actuators* B
128 488–93

[51] Pokhrel S, Simion C E, Teodorescu V S, Barsan N and
Weimar U 2009 *Adv. Funct. Mater.* **19** 1767–74

[52] Kim Y S 2009 *Sensors Actuators* B **137** 297–304

[53] Chen D and Sugahara Y 2007 *Chem. Mater.* **19** 1808

[54] Chen D, Gao L, Yasumori A, Kuroda K and Sugahara Y 2008
Small **4** 1813–22

[55] Chen D and Sugahara Y 2007 *Innov. Ceram. Sci. Eng.* **352**
85–8

[56] Papadopoulos C A, Vlachos D S and Avaritsiotis J N 1996
Sensors Actuators B **32** 61–9

[57] Xu J, Han J, Zhang Y, Sun Y and Xie B 2008 *Sensors
Actuators* B **132** 334–9

[58] Scott R W J, Yang S M, Chabanis G, Coombs N,
Williams D E and Ozin G A 2001 *Adv. Mater.* **13** 1468–72

[59] Joshi R K and Kruis F E 2006 *Appl. Phys. Lett.* **89** 153116

[60] Neri G, Bonavita A, Rizzo G, Galvagno S, Capone S and
Siciliano P 2006 *Sensors Actuators* B **114** 687–95

[61] Kudo M, Ohkawa H, Sugimoto W, Kumada N, Liu Z,
Terasaki O and Sugahara Y 2003 *Inorg. Chem.* **42** 4479–84

[62] Wu R J, Huang Y C, Yu M R, Lin T H and Hung S L 2008
Sensors Actuators B **134** 213–8

[63] Gou X, Wang G, Kong X, Wexler D, Horvat J, Yang J and
Park J 2008 *Chem.—Eur. J.* **14** 5996–6002